Experimental fracture sealing in reservoir sandstones and its relation to rock texture

Benjamin Busch [a,*], Atsushi Okamoto [b], Krassimir Garbev [c], Christoph Hilgers [a]

[a] *Department of Structural Geology and Tectonics, Institute of Applied Geosciences, Karlsruhe Institute of Technology, Adenauerring 20a, 76131, Karlsruhe, Germany*
[b] *Graduate School of Environmental Studies, Tohoku University, Aoba 6-6-20, Aramaki Aoba-ku, Sendai, 980-8579, Japan*
[c] *Department of Technical Mineralogy, Institute for Technical Chemistry, Karlsruhe Institute of Technology, Postfach 3640, 76021, Karlsruhe, Germany*

ABSTRACT

Faults and fractures are important fluid pathways in subsurface energy reservoirs. Especially in geothermal energy production, hydrocarbon production, and energy storage in the subsurface, fractures can enhance reservoir quality and production or storage potential. However, mineral precipitations often reduce available fracture apertures, and thus fracture porosity and permeability. Hydrothermal experimental setups, natural samples, and numerical simulations have been studied to great extent. In fractured sandstones, the main focus has been on only some controlling factors, e.g. fracture opening rate and the orientation of crystallographic axes in substrates. Furthermore, substrates have mostly been fairly homogeneous or sediment textures have not been explicitly considered. Here, fracture sealing experiments are performed on a homogeneous, massive marine sandstone and heterogeneous, laminated fluvial sandstone. Hydrothermal flow-through experiments are performed at 421 ± 1 °C and 30.5 ± 0.5 MPa for 72 h to compare resulting precipitated quartz cement textures on fracture surfaces on natural sandstones. Results indicate a strong impact of grain size variations associated with lamination on observed syntaxial quartz crystal dimensions on fracture surfaces. In layers of finer grain sizes, smaller cement overgrowths develop, as opposed to coarser grained laminae in the same sample. In homogeneous sandstones, the overgrowths appear more uniform, apart from the differences induced by varying c-axis orientations. Some open fracture porosity may be preserved in areas of finer grained laminae, as opposed to coarser grained laminae. Additionally, the potential to stabilize fractures by cement growth spanning the aperture could preserve fracture porosity and permeability in generally unfavorable stress regimes. Furthermore, the relative abundance of suitable syntaxial precipitation sites and additional mineral dissolution as a function of varying detrital compositions appears to influence the mineralogy of the precipitate. If samples are rich in quartz grains, the largest quantity of precipitate will be quartz, due to the large supersaturation in the input solution. If samples contain less quartz by volume, the same solution additionally precipitates phyllosilicates, implying that some structural-diagenetic mineral phases are a function of heterogeneity of the host rock, rather than a result of variable external fluid compositions entering the formation. The phyllosilicates additionally act as nucleation discontinuities, reducing the size of surfaces available for syntaxial precipitation of quartz. Results may be applicable in fractured sandstone lithologies, which have been in the focus of energy storage and production.

1. Introduction

Open fractures enhance fluid flow and are thus important structures in many applications utilizing the subsurface as energy source, such as hydrocarbons or geothermal, or for storage such as heat, hydrogen or carbon capture (Becker et al., 2018; Busch et al., 2019; Gale et al., 2014). On the other hand, they provide a risk for seal and barrier integrity for subsurface waste disposal (Tirén et al., 1999). Fractures are known to host a wide range of mineral deposits, which affect the utilization of the subsurface (e.g., Laubach et al., 2019). Hence, mineralogical alterations like dissolution or precipitation over geological timescales (e.g., Laubach et al., 2019) may profoundly affect fracture strength, openness, and the capacity to fractures to conduct fluids, with ramifications for engineering management of reservoirs and storage systems (Laubach et al., 2004). Fluid flow of supersaturated solutions in fractures may result in fracture sealing as syntaxial overgrowth on the fracture wall, depending

on the present fluid chemistries, and fluid pathways may be completely blocked (Hilgers et al., 2004; Hilgers and Tenthorey, 2004). Even small cement volumes within fracture systems connected by narrow fracture segments were shown to affect fluid flow (Philip et al., 2005). However, where opening rates are larger than the mineral growth perpendicular to the fracture surface, open porosities may be preserved (Gale et al., 2010; Hilgers et al., 2001; Lander and Laubach, 2015; Laubach, 2003; Prajapati et al., 2018a; Urai et al., 1991). This is largely influenced by the orientation of the fastest growing crystallographic axis in relation to the fracture surface (Cox and Etheridge, 1983; Hilgers and Urai, 2002; Lander and Laubach, 2015; Okamoto and Sekine, 2011). The bridging of local fracture cements may keep a fracture open even in unfavorable stress regimes and positively impacts fracture permeability (Laubach et al., 2004; Okamoto and Sekine, 2011).

The growth rate of syntaxial cement on detrital grains is controlled by the reactive surface area of the grain fabric (e.g., Lander et al., 2008). Smaller available surface area for syntaxial cementation in the pore space, i.e. smaller grains or sub-grains, results in smaller volumes of quartz cement formed over geological timescales (Lander et al., 2008; Prajapati et al., 2018b). This process has been experimentally shown to be effective for different substrate sizes exposed to the same thermal and pressure conditions over time (Lander et al., 2008). This should thus have an impact on observed cement textures in cemented fractures hosted in lithologies with varying substrate sizes (e.g. reflected by the detrital grain size).

Additionally, the detrital composition (i.e. rock fragments and mineral grains present at the deposition of the sediment) of host rocks needs to be considered. The lower the amount of quartz or quartz-containing grains in the host rock, the less surface area is available for syntaxial precipitation from silica solution, resulting in different amounts of formed syntaxial cements (see also Lander and Walderhaug, 1999). Such multi-mineral rock composition may also act as nucleation sites for additional precipitates such as clay minerals affecting reactive flow (Deng et al., 2018; Steefel, 2019).

The reactive surface area for quartz precipitation decreases, if the sandstone contains clay mineral grain coatings covering the quartz grains (Heald and Larese, 1974; Pittmann et al., 1992). Such clay mineral grain coatings prevent syntaxial overgrowth on detrital quartz grains (Busch et al., 2017), while a fractured quartz grain exposes a reactive surface.

We want to test if the different grain sizes in individual laminae affect syntaxial fracture cement precipitation as is observed in porous sandstones (e.g., Lander et al., 2008) and if the mineralogical composition of the host rock affects syntaxial cement precipitation as in metamorphic samples (e.g., Okamoto et al., 2008).

Here we show that the varying substrate grain size and detrital composition in the studied sandstone samples containing laminations of finer and coarser grains affect the volumes of syntaxially precipitated quartz cement on the fracture surface. A homogeneous sandstone sample containing little grain size variation, without prominent lamination, and above 95% quartz grain content experiencing the same hydrothermal experimental conditions are substrates to larger cement volumes than laminated sandstones containing grain size variations and having a less quartz-rich (avg. 50% quartz grains) composition.

2. Materials and methods

2.1. Samples

Homogeneous, massive sandstone samples were taken from Gildehaus Quarry in Bad Bentheim, Lower Saxony, Germany. The Bentheim sandstone is a shallow marine sandstone, deposited during the Lower Cretaceous Valanginian (Mutterlose and Bornemann, 2000). The Bentheim sandstone is a reservoir unit and also often used for geomechanical tests due to its homogeneous texture and quartz-rich composition (Klein et al., 2001; Stanchits et al., 2009; Vajdova et al.,

2004). The samples are classified as quartz arenites based on thin section analysis. Oriented 1-inch (2.51 cm) plugs (porosity: 26.1%) were drilled parallel to bedding, visible from bedding contacts in the outcrop. From 1-inch plugs, smaller, 6.5 mm diameter oriented plugs were drilled parallel to bedding (Fig. 1 b).

The second set of samples were taken from finely laminated (mm to cm-scale) sandstones containing grain size changes from a quarry near Cleebourg, Department Bas-Rhin, France (Soyk, 2015). The sandstones belong to the Grès Vosgien (Lower Triassic) and were deposited in a fluvial setting during an arid climate during the Lower Triassic Buntsandstein (Bossennec et al., 2015). Samples were retrieved from mined boulders and can be classified as subarkoses, lithic arkoses or feldspathic litharenites based on thin section analysis, and thus represent a heterogeneous host rock for the syntaxial growth of quartz on fracture surfaces. The samples show a very prominent red color with greyish-white layers. The bed from which the red and white sandstone originates is prominently visible within the outcrop. The fractured Buntsandstein is both a target for geothermal and hydrocarbon production in the Upper Rhine Graben (Bertrand et al., 2018; Bossennec et al., 2018; Haffen et al., 2013, 2015). From a hand specimen (porosity: 16.5%), ~6.5 mm plugs were drilled parallel to bedding containing both, red and white layers parallel to the long axis of the plug (Fig. 1 a). The white laminae in the generally red sandstone are a result of larger detrital grain size, lower compaction and subsequent preferential bleaching and cementation (Schmidt et al., 2020) along the more porous, now white, laminae.

The created ~6.5 mm diameter plugs were sawn into 3–5 mm thick slices. Sample surfaces were ground to an 800 grid sandpaper finish, to create similar reference surfaces in all samples, as analogs to fracture surfaces (Fig. 2 b). Ground material was cleaned from the surfaces using pressurized air. Although this might not represent a likely conchoidal intragranular fracture or detrital quartz grain surface in case of an intergranular fracture, both sample series have the same starting conditions to study precipitation on the sandstone plugs. Furthermore this favors precipitation on all ground grains and eliminates the effect of grain coating clay minerals on syntaxial precipitation (e.g., Heald and Larese, 1974). The sample holder is a 10 mm diameter half-cylinder split along the axis of the cylinder (Fig. 2 b). A hole of 7 mm diameter and 2 mm depth was milled into the planar surface to receive the samples. The samples are pressure fit using pieces of a 0.2 mm thick steel mesh. The samples in their respective holders were weighed before and after the experiment to assess the mass of precipitated silica. Of each sandstone type, one piece was prepared as a reference for SEM analyses.
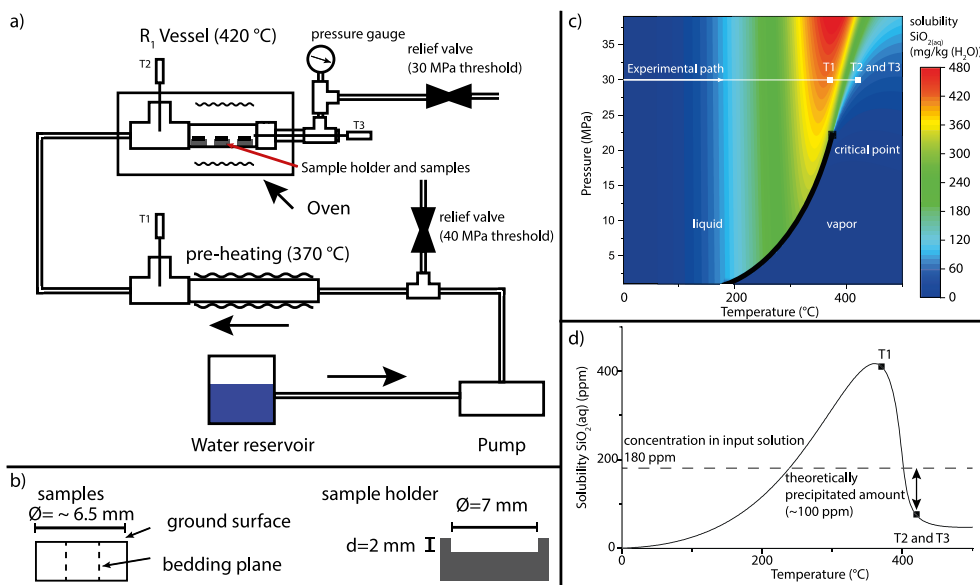
2.2. Experimental setup

The flow-through experimental setup is similar to that of Okamoto et al. (2010) and Okamoto and Sekine (2011) situated at the Graduate School of Environmental Studies, Tohoku University and is briefly described below.

The input solution is created by dissolving a mixture of quartz sand (30 g, 1–2 mm diameter) and ground granite (Iidate granite, 30 g, ~ 1–2 mm diameter) at 370 °C. The solution contains minor amounts of Al, K, and Na derived from feldspars, which have been shown to enhance the precipitation of quartz and prevent the formation of metastable polymorphs as opal-A and opal-C (Okamoto et al., 2010; Saishu et al., 2012). The resulting solution is diluted to 180 mg/kg (H_2O) SiO_2.

The input solution is filled into a Teledyne Isco 260D syringe pump used to initiate constant flow at 0.3 ml/min (Fig. 2 a). The reaction vessel in the horizontal flow path setup is made from stainless-steel (SUS316) tubes. Between the syringe pump and the pre-heating R_0 vessel, a back-pressure valve is located in case the system requires pressure release due to precipitate blocking of either of the vessels or connecting capillaries and fittings. The pre-heating (R_0) vessel is heated to 370 ± 2 °C using a heating coil, and fluid temperatures inside the vessel are monitored using thermocouple T1 (Chino Sheathed K-type
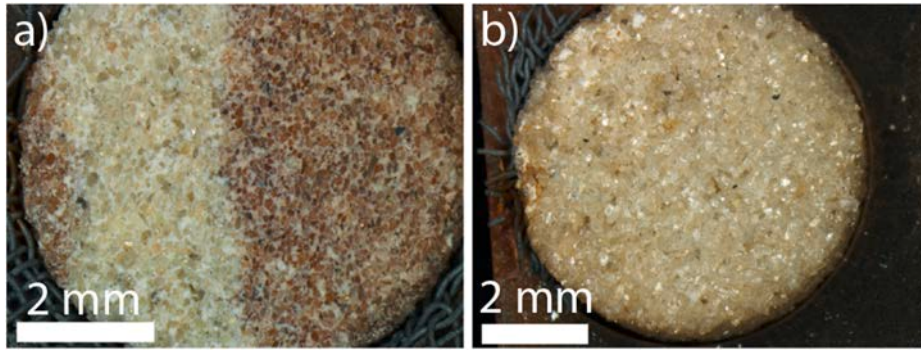
Fig. 1. Photographs of samples from Cleebourg (a, CL) and Bad Bentheim (b, BEN). CL samples are characterized by red and white lamination coinciding with grain size variations in the sandstones. BEN samples are homogeneous beige to white sandstones with no apparent lamination. (For interpretation of the references to color in this figure legend, the reader is referred to the Web version of this article.)

Fig. 2. a) Flow through experiment setup similar to Okamoto et al. (2010) and Okamoto and Sekine (2011) with three samples (black rectangles) in a row for each experiment. b) Sketch of the orientation of bedding in the respective cylindrical samples with fluid flow along the ground surface, being placed in the experimental setup in the R1 vessel. c) Quartz solubility as a function of temperature and pressure. The experimental setup is pressurized to 30.5 MPa and a flow rate of 0.3 ml/min is established. The input solution is heated to 370 °C (T1) before entering the reaction vessel. Here temperatures are 421 °C (T2 and T3) and precipitation is occurring, due to the lower solubility of quartz. The fluids are cooled before exiting the setup. Modified and adapted after Amagai et al. (2019). d) Isobaric solubility diagram of quartz at 30 MPa, showing the temperatures in the flow-through experimental setup at T1, T2 and T3 and the Si concentration of the input solution and theoretically precipitated amount at T2 and T3 (modified after Okamoto et al., 2017).

thermocouple, SUS316). The pre-heating vessel and associated downstream capillaries are placed in hollowed out isolating firebricks (Isolite A1), to prevent cooling before entering the reaction vessel (R$_1$). Following pre-heating, the solution enters the ~8 cm long R$_1$ vessel, which is placed inside a cylindrical oven. Samples on which precipitation should occur are placed inside vessel R$_1$. Inside temperatures of the reaction vessel are monitored using thermocouples T2 and T3, in the flow path before and after the samples. Syntaxial quartz overgrowths on sandstone samples were synthesized at 421 ± 1 °C and 30.5 ± 0.5 MPa fluid pressure in hydrothermal flow-through experiments run for 72 h. Silica solubility is lower at 420 °C and 30 MPa (74.98 mg/kg (H$_2$O)) than compared to 370 °C and 30 MPa (410.89 mg/kg (H$_2$O)) (Manning, 1994) and precipitation is favored in reaction vessel R$_1$ (Fig. 2 a, c, d). The pressures and temperatures are selected to achieve reaction rates, which will result in precipitation within 72 h, as in previous experimental studies (Okamoto et al., 2010, 2017; Okamoto and Sekine, 2011; Saishu et al., 2012). The downstream flow path is coiled and placed in a water bath to cool the outflow before exiting the experimental setup. Fluid pressures inside the system are monitored following the water bath and prior to a back-pressure relief valve set to 30.5 ± 0.5 MPa, which releases the fluid and maintains the internal system pressure. A fluid sample of the input solution is taken prior to the experiment. Fluid samples of the outflow solution are taken every time the syringe pump is refilled every 12 h. Samples for ICP-OES analyses are diluted 1:5 in a 3%

HNO$_3$ solution. Fluid compositions of the input solution and outflow are measured for Si, Al, Ca, Na, Mg, Fe, and K using inductively coupled plasma-optical emission spectrometry (ICP-OES; Agilent Technologies 5110) at the Graduate School of Environmental Studies, Tohoku University. The pH of untreated fluid samples is measured using a Horiba LAQUA pH-meter.

Three sample holders were placed inside the R$_1$ vessel per run. In total four runs were performed for 72 h each. Following each run the sample holders were retrieved from the R$_1$ vessel, dried, weighed and prepared for following analyses.

2.3. Analytical procedures

SEM analyses of carbon coated samples was performed using a Hitachi SU8000 Field Emission Scanning Electron Microscope (FE-SEM) located at the Graduate School of Environmental sciences, Tohoku University, using a working distance of 8 mm, an acceleration voltage of 5 kV, and a current of 10 μA. Further SEM-EDX and SEM-BSE analyses were performed on a Tescan Vega, at a working distance of 15 mm, an acceleration voltage of 15 kV and a current of 10 μA at the Department of Mineralogy and Petrology at Karlsruhe Institute of Technology.

Following SEM analyses, samples were embedded in epoxy resin to prepare polished thin sections (30 μm) for transmitted light analyses (Leica DMLP microscope fitted with a Jenoptik ProGres Gryphax Subra

camera) at Karlsruhe Institute of Technology. Thin sections are oriented perpendicular to the substrate surface.
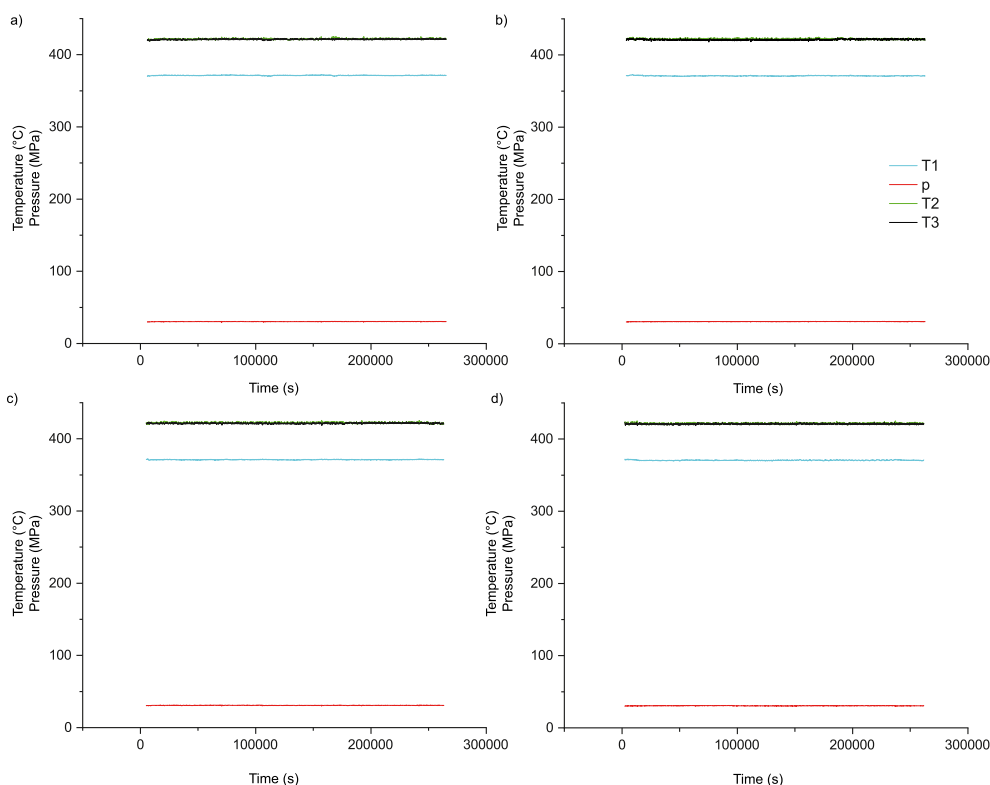
On thin section samples, the grain composition at the fracture surface was analyzed per sample utilizing line counting, to determine the amount of quartz and non-quartz grains. The substrate diameter is measured as the cut diameter of the detrital quartz grains at the artificial fracture surfaces. Crystallographic c-axis lengths were determined on crystals growing sub-perpendicular ($\pm 20°$) on the artificial fracture surface, when the c-axis orientation could be identified using digital image analysis on transmitted-light thin section images. Where the a-axis orientation could be determined, based on angles between developed facets, the length of growth parallel to the a-axis was also measured.

Confocal Raman spectroscopic analyses were employed to identify additionally precipitated minerals visible in polished thin sections. A WITec alpha300 R equipped with a Zeiss microscope and a 532 nm Laser operated at 11 mW located at the Institute of Technical Chemistry, Karlsruhe Institute of Technology was used to assess the mineralogical characteristics. Single spot measurements, as well as mappings were performed with a $100\times$ objective with a NA of 0.9. Raman mapping of an area of 30×15 μm was performed in 1 μm steps with 496 single measurements and an integration time of 6 s each. The spectra were taken with a 600 mm^{-1} grating covering the spectral range 120–3900 cm^{-1}. The spectra were evaluated with the Project 5.3 software from WITec. The resulting image represents in false colors the lateral distribution of the phases identified. The phase identification was aided by the RRUFF mineral database (Lafuente et al., 2015) integrated in the WITec True Match program.

3. Results

3.1. Saturations and fluid composition

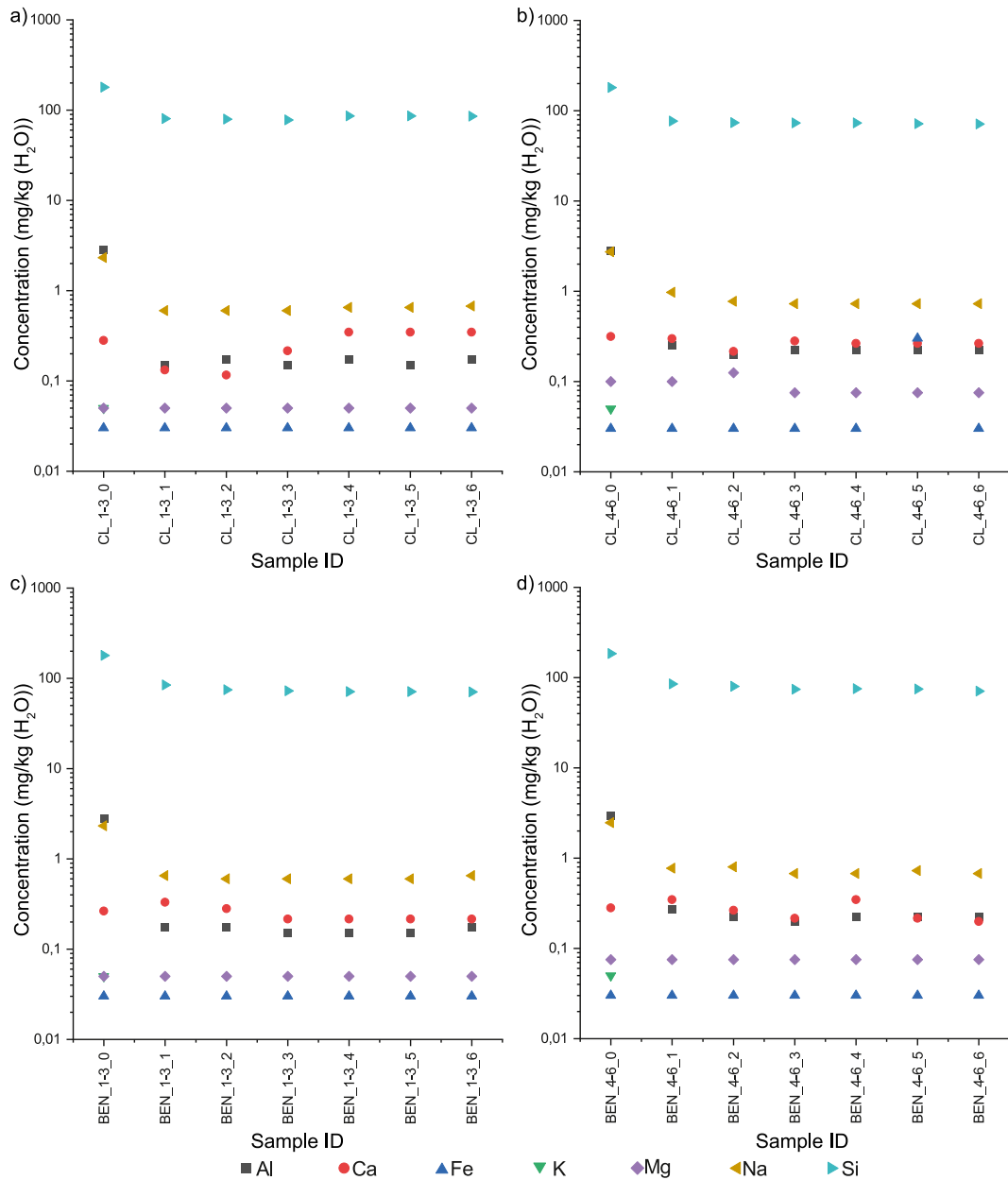The pressure and temperature data for all experimental runs show consistent experimental conditions within the reaction vessel (Fig. 3 a-d, supplementary materials, temperatures and pressures). The measured average temperature gradient between T2 and T3 was between 0.5 and 0.85 °C over a distance of 5 cm to maintain similar precipitation conditions for all samples. The resulting calculated Si solubility at average temperatures throughout the whole run at the precipitation conditions in the reaction vessel (at T2 and T3) for the four runs range from 77.23 mg/kg (H$_2$O) to 84.99 mg/kg (H$_2$O) (see supplementary materials for detailed data).

Measured fluid compositions of the input solutions used in all runs are similar (Fig. 4, supplementary materials, ICP-OES and pH). Si concentrations of the input solution are between 179.22 and 184.84 mg/kg (H$_2$O). Al, Ca, Fe, K, Mg, and Na concentrations are essentially the same. Fluid compositions after the experiment are depleted in Al, K, Na, and Si. Fe and Mg concentrations remain at low values, while Ca concentrations show some depletion and enrichment during the experiment. However, values only range from 0.12 mg/kg (H$_2$O) to 0.35 mg/kg (H$_2$O). The solution loses ~2.6 mg/kg (H$_2$O) Al, ~1.6 mg/kg (H$_2$O) Na, and 0.05 mg/kg (H$_2$O) K on average during the experiment. No changes were recorded for Fe and Mg concentrations. Fe contents were below the detection limit (<0.03 mg/kg (H$_2$O)) with the exception of one analysis (CL_4-6_5) where Fe contents in the outflow solution increase to 0.3 mg/kg (H$_2$O).

With a focus on quartz cements, the outflow solution contains between 70.9 and 86.2 mg/kg (H$_2$O) Si, thus loses approx. 100 mg/kg (H$_2$O) of Si.

The calculated supersaturation ratio for the inflow solutions of the different experiments (S   c/c*) ranges from 2.08 to 2.61 with an average of 2.37, while the supersaturation ratio of outflow solution ranges from 0.85 to 1.12 with an average of 0.95 (supplementary materials, ICP-OES and pH). The supersaturation ratio of outflow solutions is thus close to equilibrium determined for average experimental pressure and temperature conditions.

The input solution has an average pH of 7.47 (min.: 7.2, max.: 7.9,

Fig. 3. Overview of measured pressure and temperature data during the experiments plotted in 10 s intervals. a) Run CL_1-3. b) Run CL_4-6. c) Run BEN_1-3. d) Run BEN_4-6.

Fig. 4. Overview of the ICP-OES results for all four runs. The sample suffix _0 represents the composition of the initial input solution. a) CL_1-3, b) CL_4-6, c) BEN_1-3, d) BEN_4-6.

supplementary materials, ICP-OES and pH) and stays between a value of 7 and 8 throughout the experimental runs, except for two outliers in series CL_1–3 which are as low as 6.95 (supplementary materials, ICP-OES and pH).

3.2. Quartz precipitation and coprecipitates

The samples positioned further upstream (suffix _1 and _4, position 1) gained more weight, and thus more precipitate than samples further downstream in the flow through experiments (suffix _3 and _6, position 3) (Fig. 5, supplementary materials, Weight). Only between 4 and 32% by weight of precipitate formed on the upstream samples is precipitated on the downstream samples.

Differences also arise from the amount precipitated on different sample types. The homogeneous Bentheim Sandstone (BEN) contains more precipitate than the heterogeneous samples from Cleebourg (CL). On average, twice the amount was precipitated on the homogeneous

BEN samples as opposed to heterogeneous CL samples at the same position relative to the flow path.

The substrates prior to the experiments show the fracture surfaces (Fig. 6 a, b). The scanning electron microscopy observations highlight that the precipitated quartz from hydrothermal flow-through experiments show euhedral crystals of various crystallographic orientations and varying sizes. Samples from Bentheim (BEN) generally show larger crystals and a more homogeneous distribution of crystal sizes (Fig. 6 d, g). On the other hand, samples from Cleebourg (CL) generally show fewer large syntaxially overgrown quartz crystals and local differences between the white and red parts of the sample. The white laminae (Fig. 6 c, f) show larger quartz crystals than the red laminae of the sandstone (Fig. 6 c, e). CL samples additionally contain a fibrous to platy coprecipitate (Fig. 6 e, f).

In transmitted light the ground surface of the initially overgrown surface can still be observed after experimental precipitation (black arrows, Fig. 7 a, c, d), due to solid and fluid inclusion trails.
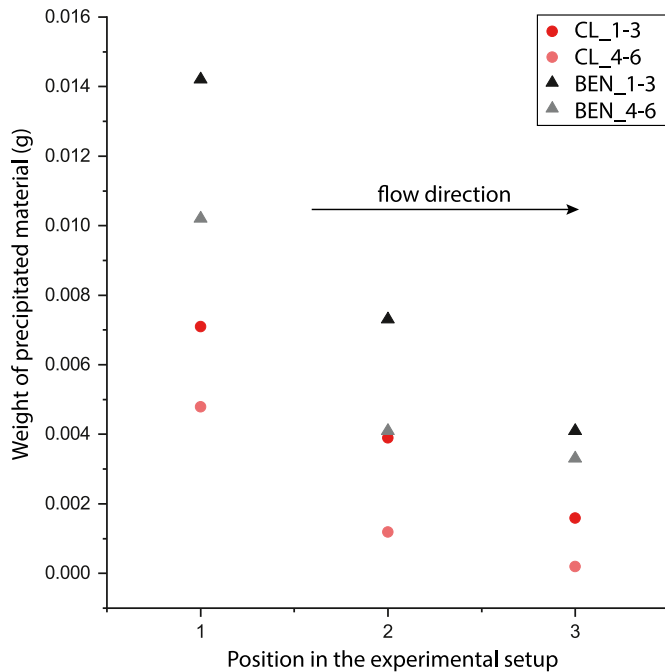
Fig. 5. Weight of precipitated material per sample at each position within the experimental setup (position: 1 – upstream, 2 – midstream, 3 – downstream).

Further light microscopic analyses on thin sections from the heterogeneous CL samples reveal the intricate control mechanism on the distribution of precipitation sites in the studied samples. While syntaxial quartz precipitates on quartz grains, non-quartz grains, such as feldspars, micas, and metamorphic rock fragments do not show a syntaxial precipitate (red stars, Fig. 7 a, b).

Homogeneous BEN samples show euhedral quartz precipitates on almost all detrital quartz grains (Fig. 7 c, d). The fracture surface is visible based on solid inclusions underneath overgrowths (black arrows, Fig. 7 c, d). The fibrous to platy coprecipitate is absent.

In transmitted light the coprecipitates are also clearly visible, partly covering the grains intersecting the fracture surface (Fig. 8 a-d, black and white arrows). Especially in areas at grain contacts precipitation appears to occur more frequently, where illitic/hematitic grain coatings (Fig. 8 a, d, green arrows) or sheet silicate-rich rock fragments and detrital micas intersect the fracture surface (Fig. 8 b, c, d, blue arrows, Fig. 7 a, b, red arrows). The fibrous to platy texture of the coprecipitate is also visible in thin sections (Fig. 8 a, black arrow). Where the fracture surfaces are mostly covered by the coprecipitate, precipitation of quartz appears to be inhibited (Fig. 8 b, d, white arrows), while on some grains, incomplete coverage by the coprecipitate allows syntaxial quartz precipitation (Fig. 8 b, d, red arrows).

3.3. Composition of coprecipitates

Additionally to the euhedral quartz precipitates on the fracture surfaces, fibrous to platy minerals coprecipitated only the heterogeneous samples CL_1 to CL_6 (Fig. 6 e. f, 7 a, b). Based on EDX analyses these coprecipitates contain all available ions from the input solution (Si, Al, Na, K, Mg, Ca) except for Fe. Based on the SEM observations, the coprecipitates appear to inhibit quartz precipitation and do locally act as a nucleation discontinuity (e.g. a grain coating), as quartz grew around the fibrous to platy coprecipitates (white arrows Fig. 9 a, b). The coprecipitate also appears to cover detrital grains (Fig. 9 c).

While the quartz and coprecipitates represent an addition of material to the sample, the fracture surface also contains some voids. These skeletal remnants of feldspar grains (Fig. 9 c, top red arrow) and some voids outlined by tangential illite (Fig. 9 c, bottom red arrow) both

indicate grain dissolution. This is supported by the rougher surface of feldspar grains observed in the thin section samples (Fig. 7 a, b), while quartz grains show a smooth surface at the ground interface (Fig. 7 c, d).

Raman spot analyses and mappings were performed on sample CL_4 showing quartz precipitates and the coprecipitate (Fig. 10 a). The Raman image of the phase distribution (Fig. 10 b) in the area of the square drawn in Fig. 10 a, shows the interface of the quartz with epoxy resin. Along with quartz and accessory TiO_2 and SiC (from sample polishing), the coprecipitate is located at the interface of the detrital quartz with the epoxy resin. In addition, some organic contamination (identified as carbon) is measured as part of the spectra.

The Raman spot analysis (black line in Fig. 10 c) in the area of the coprecipitate shows prominent bands at 198 cm^{-1}, 264 cm^{-1} and 702 cm^{-1} along with a quartz band at 462 cm^{-1}. The former bands are typical for sheet silicates of a dioctahedral type and match the spectra of paragonite ($NaAl_2(Si_3Al)O_{10}(OH)_2$) and pyrophyllite ($Al_2Si_4O_{10}(OH)_2$) shown as the green and red line, respectively (McKeown et al., 1999; Tlili et al., 1989). The dioctahedral type is confirmed by the presence of the band at 264 cm^{-1} arising from the internal vibrations of the isosceles O–H–O triangle according to Loh (1973), and by the frequency of the Si-O$_b$-Si ("b" stands for bridging oxygen) bending vibration (702 cm^{-1}) (Wang et al., 2015). The Raman spectrum of our sample in the range 300–500 cm^{-1} shows more resemblance to that of pyrophyllite lacking the intensity of the 409 cm^{-1} band typical for muscovite. This observation could be explained by possible vacancies of additional cations. On the other side, the OH range shows a strong band at 3624 cm^{-1} instead of a band at 3670 cm^{-1}, which can be assigned to symmetrical stretching vibration of OH in mica structures rather than in pyrophyllite (Wang et al., 2015). The small shifts of the Raman bands from an "ideal" muscovite spectrum and the observed broadening of the bands (especially of the 3624 cm^{-1} OH band) suggests a wider elemental composition apart from paragonite and pyrophyllite, indicating that phyllosilicates of variable mineralogy formed as coprecipitates. This is supported by the EDX-analyses (supplementary materials, EDX). Especially the lower intensity of the satellite bands around 700 cm^{-1} seen in our sample compared to the spectrum of muscovite (paragonite) implies a possible Al deficiency in tetrahedral coordination. The appearance of a low intensity band at 1115 cm^{-1} supports this suggestion. This band compared to the band at 1050 cm^{-1} observed in the spectra of muscovite is used to distinguish between muscovite and phengite (celadonite) as pointed by Li et al. (2011).

Therefore, the red areas in the Raman image in Fig. 10 b could be unambiguously attributed to mineral grains of a phyllosilicate most probably of mica (paragonite) type with variable composition and Al deficiency in the tetrahedral layer.

3.4. Reactive surface area and growth anisotropy of quartz

Samples BEN do show a linear correlation (R^2 0.98) of the number of quartz grains in the substrate in thin section versus the number of precipitates (Fig. 11 a, black). The smaller total number of quartz grains in samples CL also show a correlation toward a larger number of precipitates with more quartz substrate grains, but the coefficient of correlation is much lower (R^2 0.68) (Fig. 11 a, red). The precipitation ratio (the ratio of the number of precipitates over the number of quartz substrate grains) for samples from series BEN lies between 86 and 100%, whereas the ratio for series CL ranges only from 45 to 76% (Fig. 11 a, black). This indicates an additional control on the amount of precipitated quartz on the fracture surface.

The relative number of quartz grains (Fig. 11 b, green) in series BEN is much larger than non-quartz grains (Fig. 11 b, red). The relative number of quartz grains in series CL (Fig. 11 b, green) is more comparable to the relative number of non-quartz grains (Fig. 11 b, red), ranging between 40 and 60% each (Fig. 11 b, black).

The data shows a consistent correlation between longer (faster) c-axis growths on larger substrate diameters of the host rock (Fig. 12, light
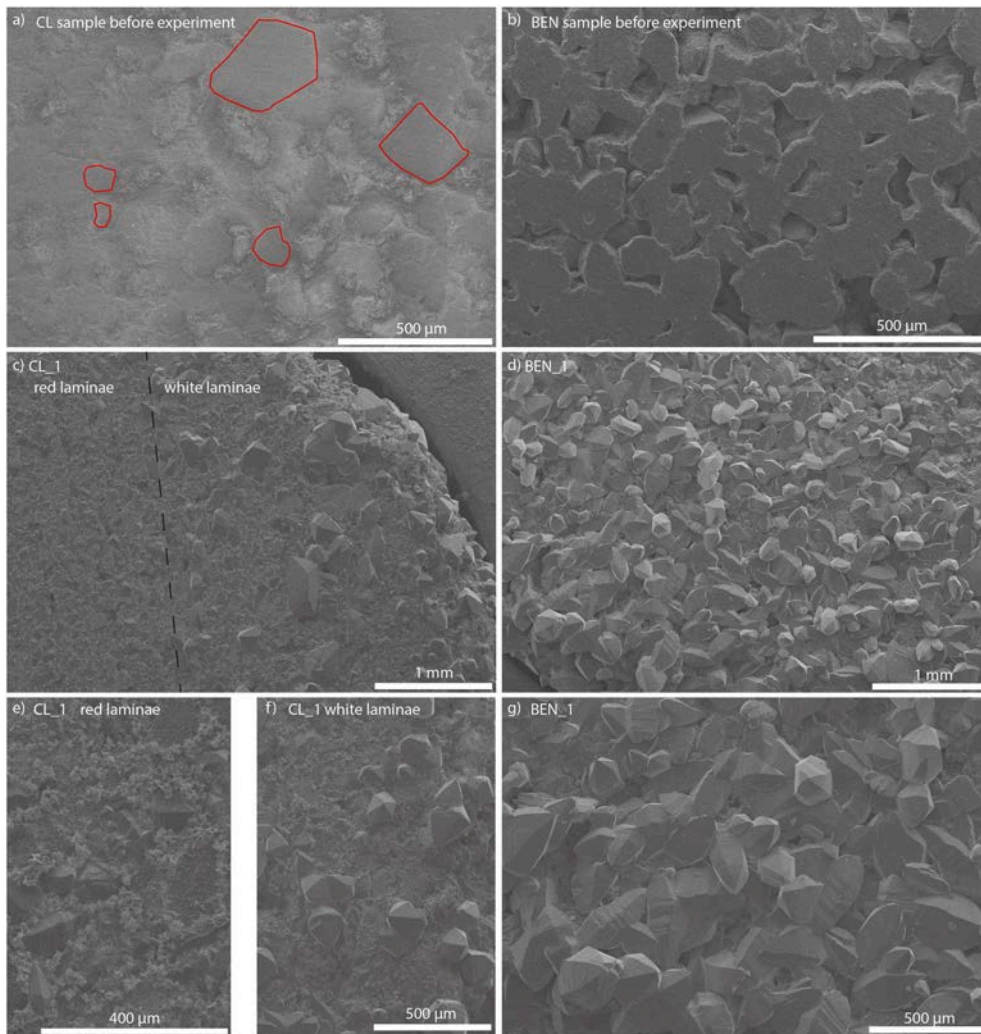
Fig. 6. SEM images of samples prior to and following the experiments. a) Fracture surface of heterogeneous CL sample. Grains of variable size have been outlined (red lines). b) Fracture surface of homogeneous BEN sample. c) Overgrown fracture surface of sample CL_1 following the experiment. The quartz crystals on the right side (white laminae) of the sample appear larger than the quartz crystals on the left side (red laminae) of the sample. d) Overgrown fracture surface of sample BEN_1 following the experiment. Equally large quartz crystals are present on all grains. e) Magnification of the red laminae of sample CL_1 showing small euhedral quartz crystals and a platy coprecipitate. f) Magnification of the white laminae of sample CL_1 showing larger euhedral quartz crystals on the fracture surface. g) Magnification of sample BEN_1 showing variably oriented equally sized quartz crystals. (For interpretation of the references to color in this figure legend, the reader is referred to the Web version of this article.)

red and grey). The R^2 of 0.75 is likely due to the use of 2D thin sections of a 3D object that likely not always cut the grain at the largest diameter or the precipitate across its maximum length. The overall finer grain size of samples from Cleebourg result in smaller overgrowths (Fig. 12, light red), but overgrowth on medium grain sized sandstone layers are within the range of c-axis lengths observed in Bentheim samples (Fig. 12, grey). Compared to the c-axes, the length of growth along the a-axes (and thus growth velocity) is much shorter and in agreement with growth rates along different crystallographic axes (Lander et al., 2008; Wendler et al., 2016). Again, larger substrate sizes correlate with longer growth along the a-axis, however the R^2 of 0.45 is poorer than for the c-axis length correlation. Generally, samples from Bentheim sandstone show longer growth along the a-axis (Fig. 12, black) than samples from Cleebourg (Fig. 12, red). The length of the axes (and thus growth velocity), derived from the upstream, midstream, and downstream region, are generally characterized by a smaller mass of precipitated material, do not reduce downstream (supplementary materials, a-axis length and c-axis length).

Overall, the relation of measured substrate size of the host rock and c-axis length of quartz precipitate, at these experimental conditions, plots close to a 1:1 correlation line (Fig. 12), while the relation of substrate size and a-axis length plots around a 3:1 correlation line (Fig. 12). This indicates a c-/a-axis growth ratio of about 3 (see also Lander et al., 2008; Wendler et al., 2016).

The average substrate diameters of quartz grains for the samples vary from 0.053 to 0.073 mm in heterogeneous samples from Cleebourg and from 0.083 to 0.120 mm in homogeneous samples of the Bentheim

sandstone. Correlating the average substrate diameters with the precipitated weight per sample results in a generally positive correlation of average substrate size and the amount of precipitates formed (Fig. 13), while the coefficient of correlation is fairly poor at R^2 0.32. However, these results are only based on the few grains intersecting the artificially created fracture surface and may not be representative for the whole sample. Furthermore, the mass of precipitate also correlates with the position within the experimental setup (Fig. 13). Samples from upstream positions (1 and 4) show a very good correlation between grain size and the weight of the precipitate.

4. Discussion

4.1. Quartz precipitation

The generated syntaxial quartz precipitates are euhedral and match overgrowths on natural samples previously synthesized in similar experimental approaches on metachert, granite, and sandstones (Okamoto and Sekine, 2011; Wendler et al., 2016). As in previous approaches, amorphous silica phases are absent (Okamoto and Sekine, 2011; Wendler et al., 2016). The c/a-axis ratio of ~3:1 is in agreement with other experimental studies (see also Lander et al., 2008). However, as the c-axis growth rate is related to substrate sizes (Lander et al., 2008, this study) (Fig. 12) a direct comparison of growth rates in mm/day along the c-axis, or precipitated weight between different experimental studies is not sensible.
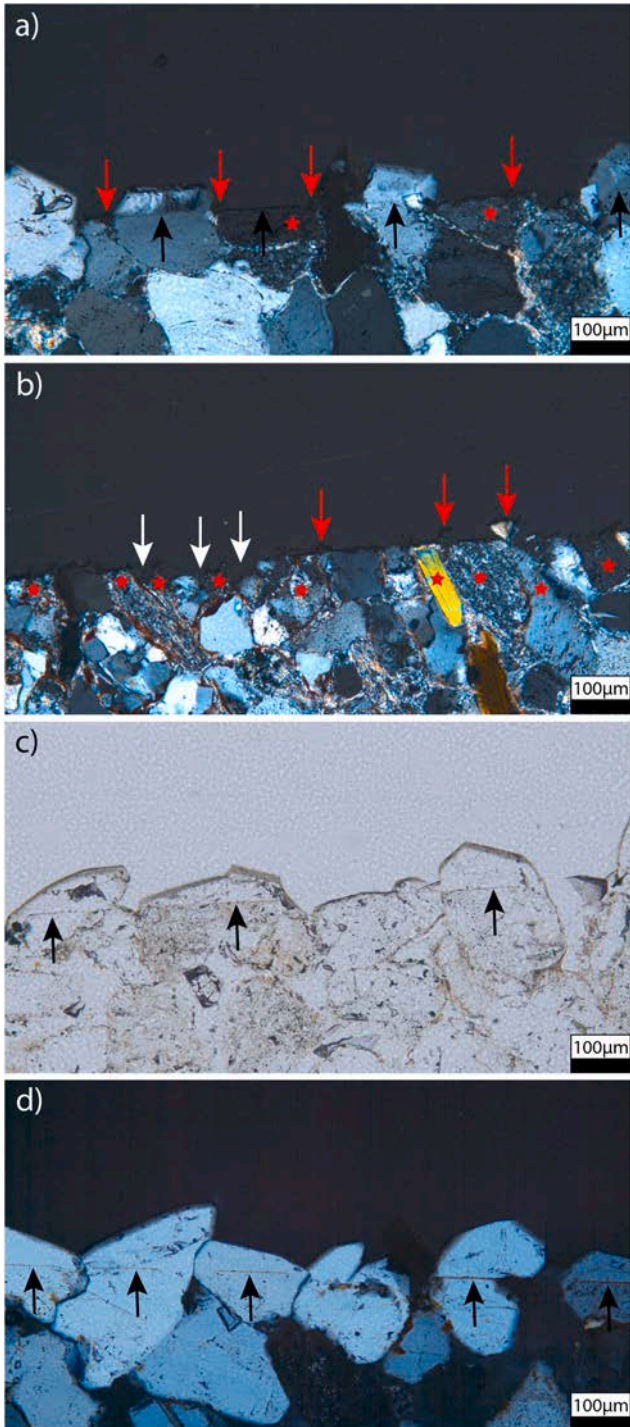
Fig. 7. a) Micrograph of the white laminae of sample CL_1 showing syntaxial quartz overgrowth on the fracture surface indicated by black arrows. No quartz precipitated on non-quartz grains (red stars = feldspars). However, some platy to fibrous mineral precipitated as well (red arrows). b) Micrograph of the red laminae of sample CL_1 showing minor amounts of quartz precipitates on the leftmost quartz grain. No quartz precipitated on non-quartz grains (red stars = micas, metamorphic rock fragments) or pore filling clay minerals. However, the platy to fibrous additional precipitate does cover most of the fracture surface and even forms larger aggregates (right red arrow). Some detrital grains appear marginally dissolved (white arrows). c + d) Syntaxial overgrowths on quartz grains (c: BEN_1, d: BEN_4). The fracture surface is indicated by the black arrows and can be seen due to reddish-brown to black solid inclusions underneath the quartz overgrowths. (For interpretation of the references to color in this figure legend, the reader is referred to the Web version of this article.)
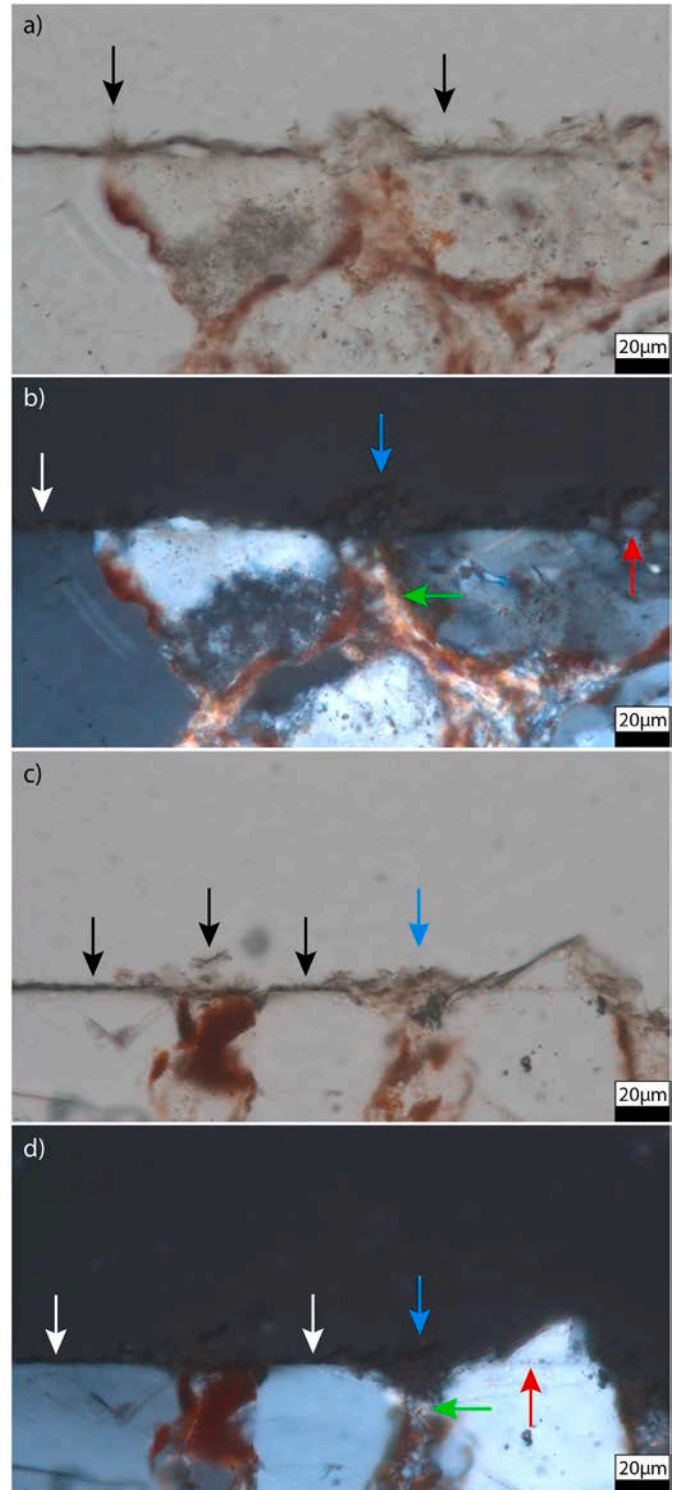
Fig. 8. The fibrous coprecipitate is present in fiber bundles at grain contacts and on the fracture surface of detrital grains and minerals (black arrows, white arrow). Especially at grain contacts containing illite (green arrow) the coprecipitate is present (blue arrows). In areas, where the ground quartz grains are not covered by the coprecipitate, syntaxial quartz precipitation is still occurring (red arrows). a, b) CL_1, ppl and xpl. c,d) CL_6, ppl and xpl. (For interpretation of the references to color in this figure legend, the reader is referred to the Web version of this article.)
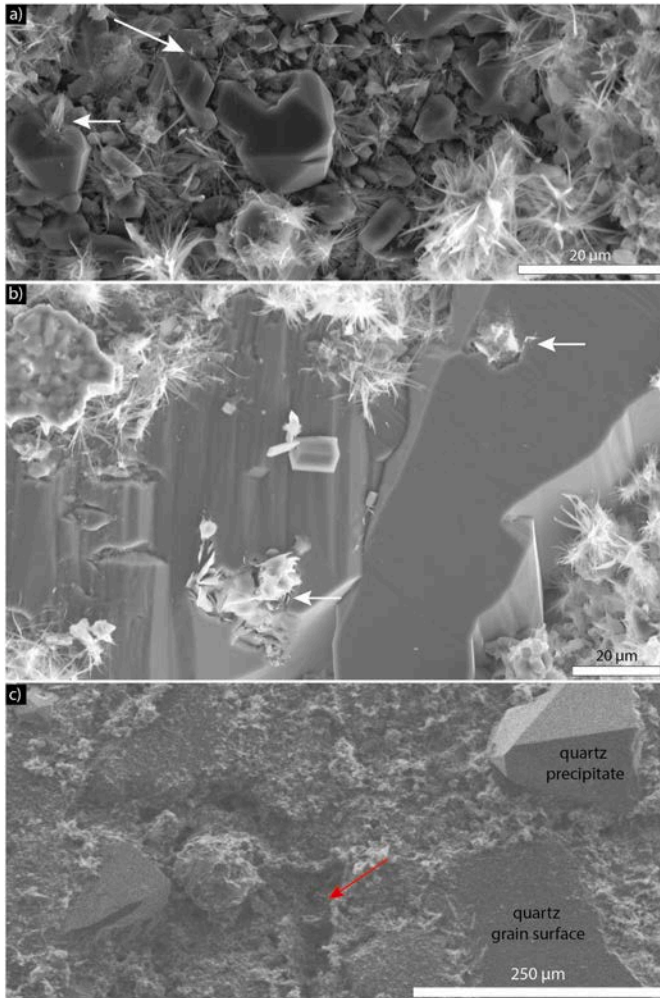
Fig. 9. a) Fibrous and platy coprecipitates form additionally to euhedral quartz overgrowths on the heterogeneous samples from the Buntsandstein (SEM-BSE, CL_4). b) The coprecipitates are occasionally encased in quartz precipitates (white arrows) and seem to act as nucleation discontinuities (SEM-BSE, CL_4). c) Void in the sample surface (red arrow) following the experiment. Skeletal remnants of dissolved grains are still recognized in the void (SEM, CL_3). (For interpretation of the references to color in this figure legend, the reader is referred to the Web version of this article.)

The c-axis and a-axis measurements allow the correlation to data derived by Lander et al. (2008), which also indicate that quartz precipitates on smaller substrates show smaller c-axis lengths than precipitates formed on larger substrates. While the correlation of c-axis length and substrate size has an R^2 0.74, the correlation of average substrate size and amount of precipitate per sample breaks down with an R^2 0.32. The anisotropy of growth rates (and thus volumes) of quartz, quantified as c-to a-axis growth ratio may still be estimated. This ratio is generally around a value of 3, derived from experimental and modeling studies (Lander et al., 2008; Prajapati et al., 2020; Wendler et al., 2016). Plotting the a- and c-axis growth length versus the substrate size (Fig. 12) results in two point clouds, which roughly follow a 1:1 (c-axes) and 3:1 (a-axes) trendline. This indicates that the difference in growth rate along these axes in the presented experiments are in the ranges previously described in literature. Including the variable orientation of crystallographic axes in natural sandstone samples can thus explain the poor correlation of the amount of precipitates and average substrate sizes per sample.

The previously established correlations of more precipitation closer to the inlet of the flow through setup (Hilgers et al., 2004; Hilgers and

Urai, 2002; Okamoto and Sekine, 2011) was also determined in the present experiments. The amount of precipitate (measured by weight) is always largest in upstream samples situated near the inlet (factor 3.1 to 4.3, one outlier with factor 25, see Fig. 5). This is related to the gradient in saturation along the flow path. Near the inlet saturations are highest, while further downstream saturations are lower as the solution contains less ions in solution due to precipitation. The average temperature gradient of 0.5–0.85 °C across the 5 cm in which the samples are situated should not significantly reduce the amount of precipitate to the present extent. While the total amounts of precipitates decreases from positions 1 to 3 (upstream to downstream), the axis lengths of individual quartz overgrowths do not correlate with the position within the reaction vessel (supplementary materials, a-axis lengths and c-axis lengths).

The composition of individual inflow solutions among the experimental runs and individual outflow solutions among the experimental runs is similar and should be a good basis to compare the resulting precipitates and relate them to observed structures and textures of the studied sandstone samples.

The observed differences in the amount and number of quartz precipitates per sample is shown to be related to the substrate grain size and detrital quartz content on the fracture surface (Fig. 11 b). The grain size, c-axis, pH, and temperature-dependent precipitation kinetics of quartz are the rate-limiting step for the amount syntaxial overgrowth, a smaller surface area available for precipitation will result in a higher silicon supersaturation of the fluid under the given conditions in the reaction vessel (Lander et al., 2008; Rimstidt and Barnes, 1980). To maintain thermodynamic equilibrium, Si will likely precipitate as a part of a different mineral species.

While published rate equations correlate the net rate of reaction ($r_{H_4SiO_4}$) to the (apparent) precipitation rate constant (k'_-) and the (super)saturation of the fluid (1-S) (e.g. eqn 36 in Rimstidt and Barnes, 1980) they do not directly include the available surface area per grain which appears to influence precipitation rates. However, results compiled by Rimstidt and Barnes (1980) state that the reaction rate is directly proportional to the interfacial area between two phases and that determined precipitation rate constants are lower for samples with on average smaller particle sizes (Rimstidt and Barnes, 1980, their Tables 2 and 3, run material 10 to 14). The specific area increases as particle size decreases in the samples consisting of quartz grains and powders (Rimstidt and Barnes, 1980, Asp in table 2). As the samples in this study do not only contain quartz grains and the amount of precipitation correlates well with individual substrate diameters, the rate decline appears to be related to the reduced surface diameters of individual substrates at the fracture and not to the overall specific surface area of quartz in the sandstone samples. The differences in the size of individual precipitation sites (substrate diameters) would explain the differing amounts of quartz precipitates on both sample series. Samples containing higher quartz contents and larger precipitation sites (BEN, avg. quartz content: 97.5%, avg. quartz substrate diameter: 0.102 mm) contain more precipitated material than samples containing lower quartz contents and smaller precipitation sites (CL, avg. quartz content: 49.2%, avg. quartz substrate diameter: 0.065 mm). This correlates well with the description of surface area normalized (SAN) growth rates derived by Lander et al. (2008) and documented in natural quartz accumulations in fractures (Laubach et al., 2019).

Calculated Si solubilities (77–84 mg/kg (H_2O)) at conditions within the reaction vessel are consistently within the range of measured Si concentrations (70–86 mg/kg (H_2O)) in outflow solutions. The initially supersaturated Si solution thus likely reached equilibrium concentrations within the reaction vessel. Slight differences may be associated to additional precipitation during cooling of the solution.

While the Si concentration of 180 mg/kg (H_2O) at the inlet may be above natural formation waters (North Sea formation waters ranging from 3 to 55 mg/kg (H_2O)) (Warren et al., 1994)), the resulting supersaturation ratio based on Si concentration measurements following the
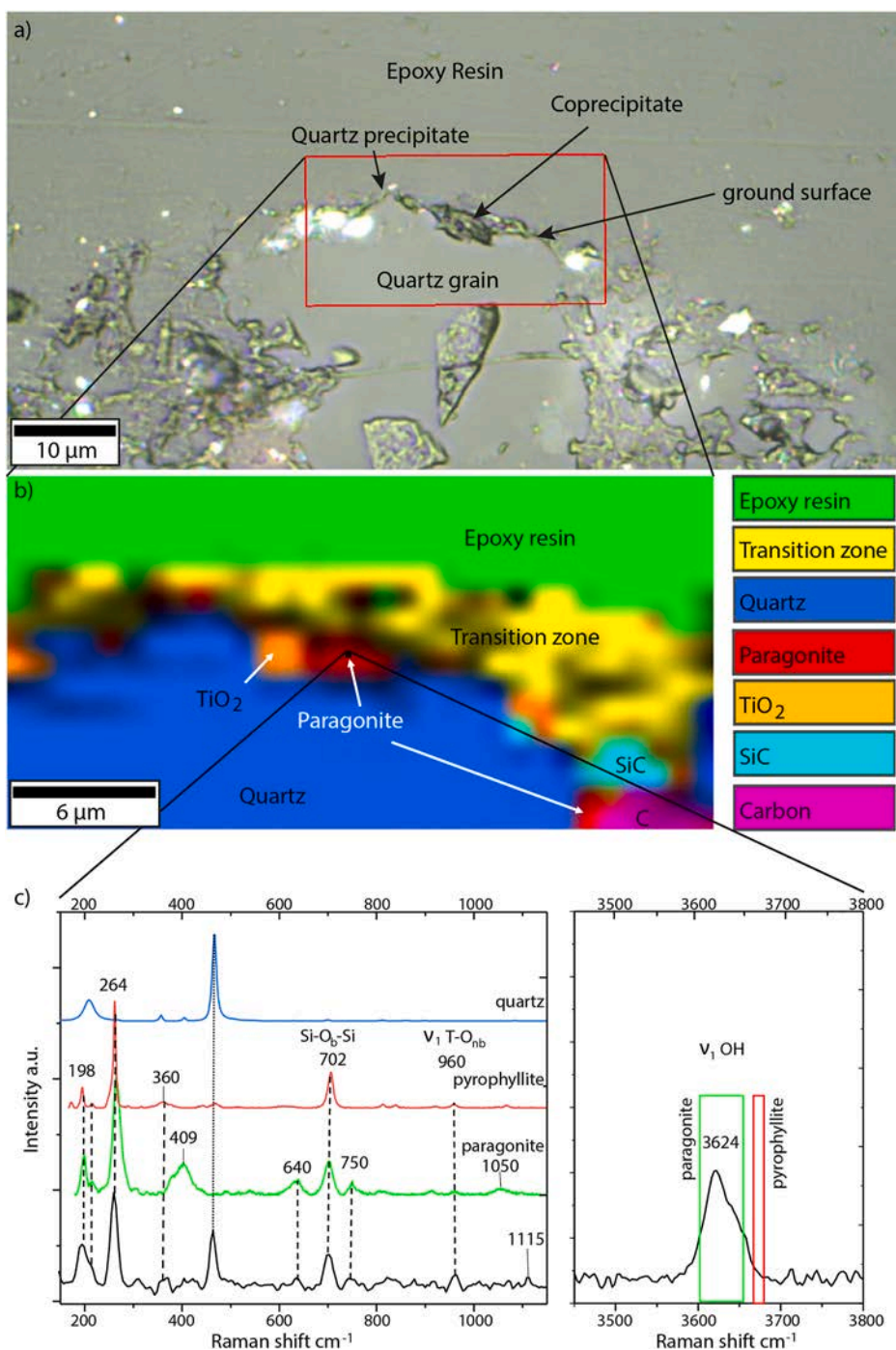
Fig. 10. Results of Raman analyses. a) Reflected light image of the area studied by Raman spectroscopy (red rectangle). b) Distribution map of the studied area highlighting areas of similar Raman spectra (1 μm spot size). c) Raman spectra of a point measurement inside the high concentration area (black) showing prominent absorption bands of quartz (blue), pyrophyllite (red), and paragonite (green) and the prominent O–H absorption band at 3624 cm^{-1}, supporting the presence of a phyllosilicate containing OH groups. Reference spectra for quartz, pyrophyllite and paragonite are extracted from the RRUFF mineral database (Lafuente et al., 2015). (For interpretation of the references to color in this figure legend, the reader is referred to the Web version of this article.)

experiments range from 2.08 to 2.61. When assessing the Si concentrations of North Sea formation waters compiled by Warren et al. (1994) and calculating Si saturations based on Manning (1994) for the given pressures and temperatures allows delineation of supersaturation ratios. The average supersaturation ratio for the given reservoirs is 0.98 (N 30, supplementary materials). However, maximum supersaturation ratios are 2.27 and 2.12 and are thus within the range of supersaturation ratios of the presented experiments. The experiments may thus be analogs for some natural reservoir systems with high supersaturation ratios. The average Si supersaturation ratio of outflow solutions is close to equilibrium (0.95) at average experimental pressure and temperature conditions during the experimental runs.

4.2. Coprecipitate

The presence of the fibrous to platy coprecipitate on the heterogeneously composed CL samples indicates that the detrital and authigenic phases present in these samples are responsible for the observed differences in single (BEN) and multiple (CL) mineral precipitates. This could be related to the mineralogical heterogeneity, which have been shown to affect reactivity (Li et al., 2006) and reactive surface area available for reactions (Beckingham et al., 2017).

The coprecipitate contains Ca, Mg, Na, Si, Al, and K. While Al, Na, K, and Si concentrations in outflow solutions are lower than in the input solution (Fig. 4), no consistent reduction in concentration could be derived for Ca and Mg, which are present in the coprecipitate based on
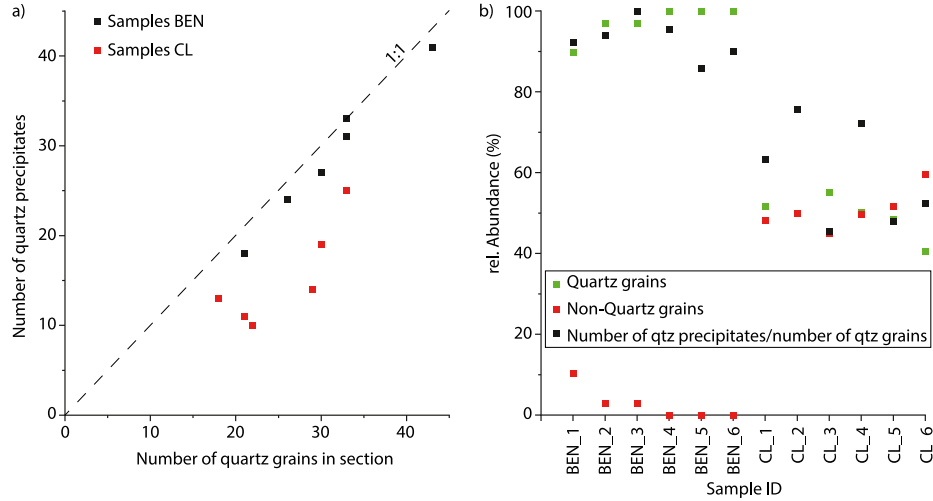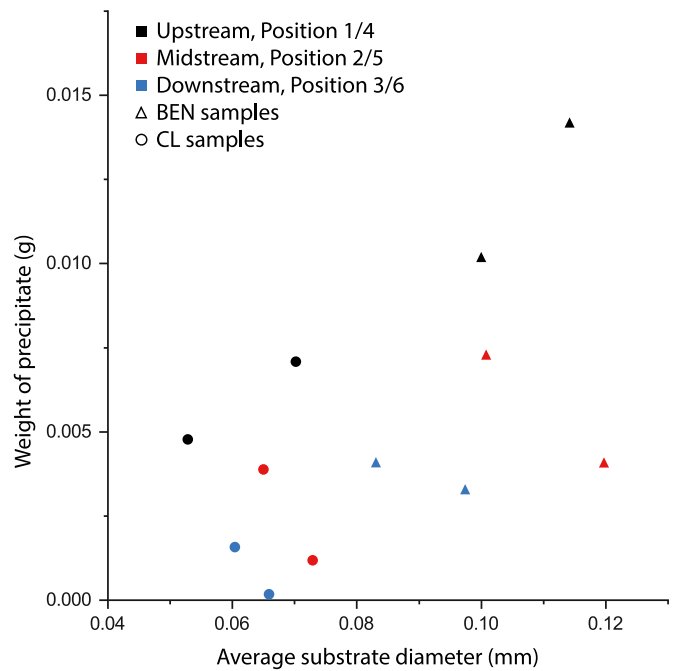
Fig. 11. a) Correlation of the number of quartz containing substrate grains versus the number of quartz precipitates derived from thin section samples. b) Number of quartz grains (green), non-quartz grains (red) and the precipitation ratio (black), showing distinct differences between the two sample series. (For interpretation of the references to color in this figure legend, the reader is referred to the Web version of this article.)
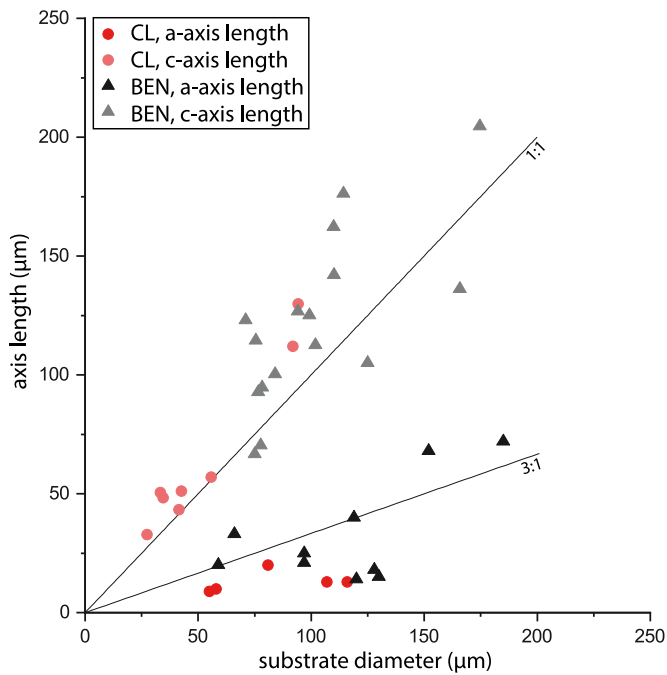
Fig. 12. Correlation of the substrate diameter of individual quartz grains and the dimension of the growth along the crystallographic a- and c-axes on the respective grains. The 1:1 and 1:3 trendlines are only applicable to the presented experimental setup and will likely change with longer durations, as crystals have more time to grow further.

Fig. 13. Correlation of average substrate diameter and mass of material precipitated for all samples color-coded for the position within the experimental setup. (For interpretation of the references to color in this figure legend, the reader is referred to the Web version of this article.)

SEM-EDX analyses. Furthermore, the initial content of Ca is below 1 mg/kg (H_2O) and of Mg is below 0.1 mg/kg (H_2O) and it is unlikely that these small contents produced this much precipitate. The same is valid for phosphorous, which was detected during SEM-EDX analyses, but should not be present in the input solution.

The likeliest source for Ca and P are apatite grains, which frequently occur as accessories in sandstones and as an authigenic phase in samples from Cleebourg (Soyk, 2015). Additional Ca and Mg could be derived from metamorphic rock fragments containing both feldspars and micas present in the studied samples (Fig. 8 d, green arrow). This can be related to the dissolution voids of feldspars and metamorphic rock fragments observed on samples after the experimental runs (Fig. 7 a, c, 9

c).

Preferential nucleation sites of the coprecipitate are illite, micas, and metamorphic rock fragments, while precipitation on other grains is also observed (Figs. 7 and 8). As these minerals and rock fragments are only present in heterogeneous sample series CL, they are interpreted to be a main control on coprecipitation. As the coprecipitate is encased by quartz and precipitates on top of syntaxial quartz precipitates (Figs. 8 and 9) the formation is interpreted to be simultaneously to quartz precipitation.

Additionally, the reduced surface area for precipitation does not allow enough quartz to precipitate from solution, while the Si supersaturation still needs to be reduced to be in equilibrium at ~80 mg/kg (H_2O) at the given conditions in the experimental setup. The logical

conclusion would be that in absence of precipitation sites for quartz growth, an additional, thermodynamically stable, phase (i.e. the mica (paragonite) type coprecipitate) will form and precipitate on the sample surface. As the solution does not show a decrease in Ca or Mg contents at the outlet (Fig. 4) an internal source of ions from within the sandstone host rock is assumed. The host rock composition not only controls the available surface area for precipitation but also controls the available additional ions from dissolution processes. The dissolution thus increases the saturation of certain elements in solution and may favor the precipitation of additional mineral species besides quartz. The mobilization is also supported by increases in Ca and Mg concentrations in the outflow solution during the experiments (Fig. 4 a and b).

Raman analyses identify a mica (paragonite) type with variable composition and Al deficiency in the tetrahedral layer. The recorded spectrum shows comparable peaks with samples recorded in databases and literature (Lafuente et al., 2015; Wang et al., 2015). However, the epoxy resin impregnation in combination with small crystal sizes results in interference when measuring Raman spectra in the studied samples. Based on the elemental composition derived from SEM-EDX analyses and the crystal habit of the coprecipitate it is most likely that other phyllosilicate minerals are also formed as coprecipitates.

The coprecipitate also appears to act as a nucleation discontinuity (grain coating). If no nucleation discontinuities are expected, the number of quartz grains intersecting the analog fracture surface and the number of overgrowth should be close to a ratio of 1. This is the case for the homogeneous BEN samples, but not observed for the heterogeneous CL samples (Fig. 11). In conjunction with SEM and optical microscopic analyses, this is assigned to the precipitation of the additional coprecipitate on the exposed surfaces of detrital grains including quartz grains (Figs. 6–9). The coprecipitate is interpreted to act as a nucleation discontinuity reducing the reactive surface area, locally inhibiting syntaxial quartz precipitation.

The effect of the coprecipitates as nucleation discontinuities appears to be as effective as in sandstones containing grain coatings (Busch et al., 2017; Monsees et al., 2020) and is held responsible for the deviation of CL samples from the 1:1 line associating the number of quartz grains with the number of quartz precipitates (Fig. 11).

While generally the Fe content of the input solution is low, one sample shows an increase in Fe content during one experimental run. This could be related to the oxidation of the sample holders within the reaction vessel, showing rust development on their surface (Fig. 1 b, left side), as the hematite, which produces the red stain in thin section analyses is still prominently visible in the samples after the experiments (Fig. 8).

Coprecipitation of multiple mineral phases may be common as also documented in natural samples containing coprecipitation of quartz and ankerite (Lander and Laubach, 2015) and quartz and calcite (Laubach et al., 2019).

4.3. Implications for subsurface reservoirs

Results indicate that the detrital composition, controlling the quartz grain content, and grain size variations in laminae can be additional controls on vein cement textures in sandstones in addition to previously derived controls. These previously derived controls are mainly the c-axis orientation relative to the fracture surface (Figs. 6–8) (Hilgers and Urai, 2002; Lander and Laubach, 2015; Okamoto and Sekine, 2011), and fracture opening rate and increments, as well as total opening width (Lander and Laubach, 2015). Large crystals might span the entire fracture and could preserve fracture porosity in deeply buried sandstones, which are discussed to be targets for hydrocarbon and geothermal reservoir systems. This is favored for large grain sizes in homogeneous sandstones, while fine-grained laminae preserve additional fracture porosity due to smaller overgrowth volumes (Fig. 14) in relation to variable opening rates and increments. The overall volume of quartz cement formed in fractures hosted in laminated sandstones containing
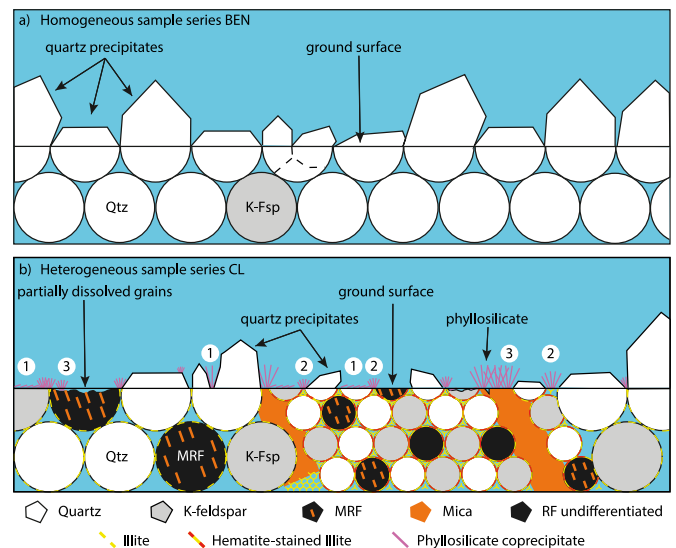
Fig. 14. Schematic sketch of experimental results. a) Quartz precipitates on homogeneous BEN samples showing equally sized overgrowths in relation to the substrate diameter. b) Quartz and phyllosilicate precipitates on heterogeneous CL samples. Smaller quartz overgrowths form on smaller grains, while larger grains are substrates to larger syntaxial overgrowths. A phyllosilicate coprecipitate forms on all detrital grains (1), but especially in areas where pore-lining and pore-filling clay minerals (2) and detrital micas including metamorphic rock fragments (MRF) (3) are present. The phyllosilicate acts as a nucleation discontinuity (grain coating) visible where encased in syntaxial quartz precipitates or inhibiting precipitation. The partial dissolution of feldspar and metamorphic rock fragments containing micas is visible in some areas, likely supplying additional ions for the precipitation of the phyllosilicates. RF: rock fragment.

grain size variations over time should thus be less than on coarser grained layers. Additionally, a less mature detrital composition reduces the number of syntaxial precipitates on fracture surfaces (Fig. 14 a, b).

Experiments have shown that additional precipitates form from the same fluid due to fluid-rock interactions in sandstones. This might be related to natural samples, as e.g. Wüstefeld et al. (2017) show chlorite growth on or near the host rock – quartz vein interface, which may be a result of precipitation from the same fluid in the absence of suitably large precipitation sites and initial host rock dissolution at the beginning of fracture cementation. The integration of structural and diagenetic processes (e.g., Laubach et al., 2010), may thus be used to reconstruct paleo-fluid compositions and processes, supported by this experimental work and may aid in identifying suitable flow pathways in present day reservoir scenarios if implemented into modeling workflows. While fibrous phyllosilicates growing into pore spaces and bridging them have been shown to negatively affect permeability in sandstones (Howard, 1992), their effect on fracture permeability has to be evaluated further. Processes like phyllosilicate migration in response to fluid chemistry changes may also result in permeability changes as a result of plugging (Cheng and Milsch, 2020) and may require additional research with a focus on fractures.

However, as ground pieces of sandstone were used as analogs for fracture surfaces some simplifications have to be kept in mind when assessing these results for natural systems. Especially the presence of clay mineral coatings often present on detrital grain surfaces in sandstones inhibit quartz cementation (e.g., Busch, 2020; Busch et al., 2018; Busch et al., 2020). Missing nucleation sites may thus allow higher silicon supersaturation in the pore fluid. Thus, transgranular fractures of quartz create reactive surface areas causing syntaxial overgrowth. In contrast, intergranular fractures do not increase the available surface area and clay mineral coatings are maintained. As a result, the cementation of intergranular fractures within well-coated sandstones by quartz

will likely be less. This effect was recently also discussed to be effective in limestone to form variable fracture cement patterns (Spruženiece et al., 2021).

While the temperature at which experiments were performed is higher than in most subsurface reservoirs, they may be comparable to those of supercritical geothermal reservoirs (Saishu et al., 2014; Scott and Driesner, 2018). While the elevated temperatures likely increases the precipitation rates, as derived for natural sandstone samples from Norway (Walderhaug, 1994), the observed quartz cement textures are comparable to fractured sandstones, where small euhedral precipitates from rinds in open fractures (Laubach et al., 2016, their Fig. 9). Fluid inclusion analyses by Laubach et al. (2016) in their set 1 fracture precipitates reveal temperatures ranging from 142.5 to 165.5 °C. This supports that the observed experimentally formed quartz cement textures can also be formed in lower temperature natural settings.

The dimensionless Péclet and Damkohler numbers aid in assessing the relative importance of transport mechanisms governing overall solute transport (e.g., Dijk and Berkowitz, 1998). The Péclet number (Pe) describes the relation between advection and diffusion rate, while the Damkohler number (Da) describes the relation of reaction rate to diffusion rate (Dijk and Berkowitz, 1998). With the diffusivity of Si in supercritical water, as in this and previous experimental setups (Wendler et al., 2016), derived from literature (5×10^{-8} m^2 s^{-1}) (Walton, 1960) gives Pe 11, while including the average quartz growth velocity of 4×10^{-10} m s^{-1} gives Da 2.7 $\times 10^{-3}$. These values are slightly larger than derived by Wendler et al. (2016) but also indicate diffusion to be faster than crystal growth, while advection is slightly faster than diffusion rates. Thus, the crystallization process is dominated by interface kinetics and not solute transport as also derived in previous studies (e.g., Okamoto et al., 2010).

Apart from indications on possible controls on syntaxial fracture cementation in sandstones, these experiments could also highlight the coeval precipitation of quartz overgrowths and phyllosilicates in sandstones, which may be applicable to diagenetic systems. The available amount of reactive surface area of quartz appears to control additional mineral precipitation in addition to supplementary ions sourced from the dissolution of detrital and authigenic phases. This in turn could explain laminae or bed-bound differences in authigenic mineral assemblages related to fluid-rock interactions with the same fluid at the same pressure and temperature conditions. Similar observations of varying mineral distributions in natural veins relating to compositional banding of the host rock were made by Okamoto et al. (2008) in pelitic schists. Furthermore, differences is quartz accumulations have also previously been related to differences in host rock compositions (Laubach et al., 2014). This implies that cementation (in diagenetic and structural diagenetic systems) is not only related to the fluid composition but fluid-rock interactions.

5. Conclusions

Reactive-flow precipitation experiments of quartz in sandstones show decreasing growth downstream. At constant flow rates and similar supersaturations only 4–32% of the amount precipitated on the upstream sample is precipitated on the downstream sample.

The microstructural composition of two different sandstones' detrital quartz grain size and reactive surface area have a profound effect on the quartz precipitation and coprecipitates. The relative abundance of available precipitation sites and precipitation rate declines in relation to decreasing detrital grain size. Grain dissolution supplying additional cations additionally appears to influence the precipitation of additional mineral phases.

The size of the substrate grains controls the volume of precipitate formed on each grain. Smaller grains form smaller overgrowths (avg. substrate diameter in CL samples: 0.053 mm, avg. c-axis length in CL samples: 0.066 mm), while larger grains are substrates to larger precipitates (avg. substrate diameter in BEN samples: 0.102 mm, avg. c-axis

length in BEN samples: 0.122 mm), likely indicating differences in the volume of quartz cement growth in fractures hosted in sandstones with varying grain sizes at suitable thermal exposures. Nevertheless, the c/a-axis growth ratio of ~3:1 outlined by previous studies could also be delineated.

Where a small numbers of precipitation sites are available and grain dissolution occurs, coprecipitation of quartz and phyllosilicates is observed. These phyllosilicates additionally appear to locally inhibit precipitation on quartz grains acting as a nucleation discontinuity similar to grain coating clay minerals. This process could aid in the assessment of structural diagenetic mineral assemblages in geological systems and aid in the assessment of fluid flow systems affected by mineral precipitation.

Including these results in modeling approaches may aid in identifying and predicting fluid pathways in fractured lithologies with a variable thermal exposure, leading to fracture sealing by quartz precipitation or preservation based on the lower growth rates on smaller substrates.

References

Amagai, T., Okamoto, A., Niibe, T., Hirano, N., Motomiya, K., Tsuchiya, N., 2019. Silica nanoparticles produced by explosive flash vaporization during earthquakes. Sci. Rep. 9, 9738. https://doi.org/10.1038/s41598-019-46320-7.

Becker, I., Koehrer, B., Waldvogel, M., Jelinek, W., Hilgers, C., 2018. Comparing fracture statistics from outcrop and reservoir data using conventional manual and t-LiDAR derived scanlines in Ca2 carbonates from the Southern Permian Basin, Germany. Mar. Petrol. Geol. 95, 228–245. https://doi.org/10.1016/j.marpetgeo.2018.04.021.

Beckingham, L.E., Steefel, C.I., Swift, A.M., Voltolini, M., Yang, L., Anovitz, L.M., Sheets, J.M., Cole, D.R., Kneafsey, T.J., Mitnick, E.H., Zhang, S., Landrot, G., Ajo-Franklin, J.B., DePaolo, D.J., Mito, S., Xue, Z., 2017. Evaluation of accessible mineral surface areas for improved prediction of mineral reaction rates in porous media. Geochem. Cosmochim. Acta 205, 31–49. https://doi.org/10.1016/j.gca.2017.02.006.

Bertrand, L., Jusseaume, J., Géraud, Y., Diraison, M., Damy, P.-C., Navelot, V., Haffen, S., 2018. Structural heritage, reactivation and distribution of fault and fracture network

in a rifting context: case study of the western shoulder of the Upper Rhine Graben. J. Struct. Geol. 108, 243–255. https://doi.org/10.1016/j.jsg.2017.09.006.

Bossennec, C., Géraud, Y., Moretti, I., Mattioni, L., Stemmelen, D., 2018. Pore network properties of sandstones in a fault damage zone. J. Struct. Geol. 110, 24–44. https://doi.org/10.1016/j.jsg.2018.02.003.

Bossennec, C., Moretti, I., Geraud, Y., Mattioni, L., Daniel, J.-M., Haffen, S., Bourlange, S., Diraison, M., Malartre, F., 2015. Diagenetic features of Buntsandstein Sandstones of the eastern border of the Upper Rhine Graben and implications in terms of burial history, 15E Congrès Français de Sédimentologie, Chambéry, France.

Busch, B., 2020. Pilot study on provenance and depositional controls on clay mineral coatings in active fluvio-eolian systems, western USA. Sediment. Geol. 406, 105721. https://doi.org/10.1016/j.sedgeo.2020.105721.

Busch, B., Adelmann, D., Hilgers, C., 2018. Reservoir Quality Modeling in Deeply-Buried Permian Rotliegendes Sandstones, N-Germany. Impact of Illite Textures, EAGE Conference and Exhibition. EAGE, Copenhagen, pp. 1–5. https://doi.org/10.3997/2214-4609.201801135.

Busch, B., Becker, I., Koehrer, B., Adelmann, D., Hilgers, C., 2019. Porosity evolution of two Upper Carboniferous tight-gas-fluvial sandstone reservoirs: impact of fractures and total cement volumes on reservoir quality. Mar. Petrol. Geol. 100, 376–390. https://doi.org/10.1016/j.marpetgeo.2018.10.051.

Busch, B., Hilgers, C., Adelmann, D., 2020. Reservoir quality controls on Rotliegend fluvio-aeolian wells in Germany and The Netherlands, Southern Permian Basin – impact of grain coatings and cements. Mar. Petrol. Geol. 112, 104075. https://doi.org/10.1016/j.marpetgeo.2019.104075.

Busch, B., Hilgers, C., Gronen, L., Adelmann, D., 2017. Cementation and structural diagenesis of fluvio-aeolian Rotliegend sandstones, northern England. J. Geol. Soc. 174, 855–868. https://doi.org/10.1144/jgs2016-122.

Cheng, C., Milsch, H., 2020. Permeability variations in illite-bearing sandstone: effects of temperature and NaCl fluid salinity. J. Geophys. Res. 125 https://doi.org/10.1029/2020jb020122.

Cox, S.F., Etheridge, M.A., 1983. Crack-seal fibre growth mechanisms and their significance in the development of oriented layer silicate microstructures. Tectonophysics 92, 147–170. https://doi.org/10.1016/0040-1951(83)90088-4.

Deng, H., Steefel, C.I., Molins, S., DePaolo, D., 2018. Fracture evolution in multimineral systems: the role of mineral composition, flow rate, and fracture aperture heterogeneity. ACS Earth Space Chem. 2, 112–124. https://doi.org/10.1021/acsearthspacechem.7b00130.

Dijk, P., Berkowitz, B., 1998. Precipitation and dissolution of reactive solutes in fractures. Water Resour. Res. 34, 457–470. https://doi.org/10.1029/97WR03238.

Gale, J.F.W., Lander, R.H., Reed, R.M., Laubach, S.E., 2010. Modeling fracture porosity evolution in dolostone. J. Struct. Geol. 32, 1201–1211. https://doi.org/10.1016/j.jsg.2009.04.018.

Gale, J.F.W., Laubach, S.E., Olson, J.E., Eichhubl, P., Fall, A., 2014. Natural Fractures in shale: a review and new observations. AAPG (Am. Assoc. Pet. Geol.) Bull. 98, 2165–2216. https://doi.org/10.1306/08121413151.

Haffen, S., Géraud, Y., Diraison, M., 2015. Geothermal, Structural and Petrophysical Characteristics of Buntsandstein Sandstone Reservoir (Upper Rhine Graben, France). World Geothermal Congress 2015, Melbourne, Australia.

Haffen, S., Géraud, Y., Diraison, M., Dezayes, C., 2013. Fluid-flow Zones in a Geothermal Sandstone Reservoir: Localization from Thermal Conductivity and Temperature Logs, Borehole EPS1 (Soultz-sous-Forêts,France) and 3D Models, Thirty-Eighth Workshop on Geothermal Reservoir Engineering. Stanford University, Stanford, California.

Heald, M.T., Larese, R.E., 1974. Influence of coatings on quartz cementation. J. Sediment. Petrol. 44, 1269–1274. https://doi.org/10.1306/212F6C94-2B24-11D7-8648000102C1865D.

Hilgers, C., Dilg-Gruschinski, K., Urai, J.L., 2004. Microstructural evolution of syntaxial veins formed by advective flow. Geology 32, 261. https://doi.org/10.1130/g20024.1.

Hilgers, C., Kohn, D., Bons, P.D., Urai, J.L., 2001. Development of crystal morphology during unitaxial growth in a progressively widening vein: II. Numerical simulations of the evolution of antitaxial fibrous veins. J. Struct. Geol. 23, 873–885. https://doi.org/10.1016/S0191-8141(00)00160-7.

Hilgers, C., Tenthorey, E., 2004. Fracture sealing of quartzite under a temperature gradient: experimental results. Terra. Nova 16, 173–178. https://doi.org/10.1111/j.1365-3121.2004.00545.x.

Hilgers, C., Urai, J.L., 2002. Experimental study of syntaxial vein growth during lateral fluid flow in transmitted light: first results. J. Struct. Geol. 24, 1029–1043.

Howard, J.J., 1992. Influence of authigenic-clay minerals on permeability. In: Houseknecht, D.W., Pittman, E.D. (Eds.), Origin, Diagenesis, and Petrophysics of Clay Minerals in Sandstone. SEPM, Tulsa, Oklahoma, USA, pp. 257–264.

Klein, E., Baud, P., Reuschlé, T., Wong, T.-F., 2001. Mechanical behaviour and failure mode of Bentheim sandstone under triaxial compression. Phys. Chem. Earth 26, 21–25.

Lafuente, B., Downs, R.T., Yang, H., Stone, N., 2015. The power of databases: the RRUFF project. In: Armbruster, T., Danisi, R.M. (Eds.), Highlights in Mineralogical Crystallography. W. De Gruyter, Berlin, Germany, pp. 1–30.

Lander, R.H., Larese, R.E., Bonnell, L.M., 2008. Toward more accurate quartz cement models: the importance of euhedral versus noneuhedral growth rates. AAPG (Am. Assoc. Pet. Geol.) Bull. 92, 1537–1563. https://doi.org/10.1306/07160808037.

Lander, R.H., Laubach, S.E., 2015. Insights into rates of fracture growth and sealing from a model for quartz cementation in fractured sandstones. Geol. Soc. Am. Bull. 127, 516–538. https://doi.org/10.1130/b31092.1.

Lander, R.H., Walderhaug, O., 1999. Predicting porosity through simulating sandstone compaction and quartz cementation. AAPG (Am. Assoc. Pet. Geol.) Bull. 83, 433–449. https://doi.org/10.1306/00AA9BC4-1730-11D7-8645000102C1865D.

Laubach, S.E., 2003. Practical approaches to identifying sealed and open fractures. AAPG (Am. Assoc. Pet. Geol.) Bull. 87, 561–579. https://doi.org/10.1306/11060201106.

Laubach, S.E., Eichhubl, P., Hargrove, P., Ellis, M.A., Hooker, J.N., 2014. Fault core and damage zone fracture attributes vary along strike owing to interaction of fracture growth, quartz accumulation, and differing sandstone composition. J. Struct. Geol. 68, 207–226. https://doi.org/10.1016/j.jsg.2014.08.007.

Laubach, S.E., Eichhubl, P., Hilgers, C., Lander, R.H., 2010. Structural diagenesis. J. Struct. Geol. 32, 1866–1872. https://doi.org/10.1016/j.jsg.2010.10.001.

Laubach, S.E., Fall, A., Copley, L.K., Marrett, R., Wilkins, S.J., 2016. Fracture porosity creation and persistence in a basement-involved laramide fold, upper cretaceous frontier formation, green river basin, USA. Geol. Mag. 153, 887–910. https://doi.org/10.1017/s0016756816000157.

Laubach, S.E., Lander, R.H., Criscenti, L.J., Anovitz, L.M., Urai, J.L., Pollyea, R.M., Hooker, J.N., Narr, W., Evans, M.A., Kerisit, S.N., Olson, J.E., Dewers, T., Fisher, D., Bodnar, R., Evans, B., Dove, P., Bonnell, L.M., Marder, M.P., Pyrak-Nolte, L., 2019. The role of chemistry in fracture pattern development and opportunities to advance interpretations of geological materials. Rev. Geophys. 57, 1065–1111. https://doi.org/10.1029/2019rg000671.

Laubach, S.E., Olson, J.E., Gale, J.F.W., 2004. Are open fractures necessarily aligned with maximum horizontal stress? Earth Planet Sci. Lett. 222, 191–195. https://doi.org/10.1016/j.epsl.2004.02.019.

Li, H., Zhang, L., Christy, A.G., 2011. The correlation between Raman spectra and the mineral composition of muscovite and phengite. Ultrahigh-Pressure Metamorphism 187–212. https://doi.org/10.1016/b978-0-12-385144-4.00006-0.

Li, L., Peters, C.A., Celia, M.A., 2006. Upscaling geochemical reaction rates using pore-scale network modeling. Adv. Water Resour. 29, 1351–1370. https://doi.org/10.1016/j.advwatres.2005.10.011.

Loh, E., 1973. Optical vibrations in sheet silicates. J. Phys. C Solid State Phys. 6, 1091–1104. https://doi.org/10.1088/0022-3719/6/6/022.

Manning, C.E., 1994. The solubility of quartz in H2O in the lower crust and upper mantle. Geochem. Cosmochim. Acta 58, 4831–4839.

McKeown, D.A., Bell, M.I., Etz, E.S., 1999. Vibrational analysis of the dioctahedral mica: 2M1 muscovite. Am. Mineral. 48, 1041–1048. https://doi.org/10.2138/am-1999-7-806.

Monsees, A.C., Busch, B., Schoner, N., Hilgers, C., 2020. Rock typing of diagenetically induced heterogeneities – a case study from a deeply-buried clastic Rotliegend reservoir of the Northern German Basin. Mar. Petrol. Geol. 113, 104163. https://doi.org/10.1016/j.marpetgeo.2019.104163.

Mutterlose, J., Bornemann, A., 2000. Distribution and facies patterns of Lower Cretaceous sediments in northern Germany: a review. Cretac. Res. 21, 733–759. https://doi.org/10.1006/cres.2000.0232.

Okamoto, A., Kikuchi, T., Tsuchiya, N., 2008. Mineral distribution within polymineralic veins in the Sanbagawa belt, Japan: implications for mass transfer during vein formation. Contrib. Mineral. Petrol. 156, 323–336. https://doi.org/10.1007/s00410-008-0288-y.

Okamoto, A., Saishu, H., Hirano, N., Tsuchiya, N., 2010. Mineralogical and textural variation of silica minerals in hydrothermal flow-through experiments: implications for quartz vein formation. Geochem. Cosmochim. Acta 74, 3692–3706. https://doi.org/10.1016/j.gca.2010.03.031.

Okamoto, A., Sekine, K., 2011. Textures of syntaxial quartz veins synthesized by hydrothermal experiments. J. Struct. Geol. 33, 1764–1775. https://doi.org/10.1016/j.jsg.2011.10.004.

Okamoto, A., Yamada, R., Saishu, H., Tsuchiya, N., 2017. Porosity and permeability evolution induced by precipitation of silica under hydrothermal conditions. Proc. Earth Planetary Sci. 17, 249–252. https://doi.org/10.1016/j.proeps.2016.12.046.

Philip, Z.G., Jennings, J.W., Olson, J.E., Laubach, S.E., Holder, J., 2005. Modeling coupled fracture-matrix fluid flow in geomechanically simulated fracture networks. SPE Reservoir Eval. Eng. 8, 300–309. https://doi.org/10.2118/77340-PA.

Pittmann, E.D., Larese, R.E., Heald, M.T., 1992. Clay coats : occurrence and relevance to preservation of porosity in sandstones. In: Houseknecht, D.W., Pittmann, E.D. (Eds.), Origin, Diagenesis, and Petrophysics of Clay Minerals in Sandstones. SEPM Special Publication, Tulsa, Oklahoma, U.S.A., pp. 241–256. https://doi.org/10.2110/pec.92.47.0241

Prajapati, N., Gonzales, A.A., Selzer, M., Nestler, B., Busch, B., Hilgers, C., 2020. Quartz cementation in polycrystalline sandstone: insights from phase-field simulations. JGR. https://doi.org/10.1029/2019JB019137.

Prajapati, N., Selzer, M., Nestler, B., Busch, B., Hilgers, C., 2018a. Modeling fracture cementation processes in calcite limestone: a phase-field study. Geoth. Energy 6, 15. https://doi.org/10.1186/s40517-018-0093-4.

Prajapati, N., Selzer, M., Nestler, B., Busch, B., Hilgers, C., Ankit, K., 2018b. Three-dimensional phase-field investigation of pore space cementation and permeability in quartz sandstone. J. Geophys. Res. https://doi.org/10.1029/2018jb015618.

Rimstidt, J.D., Barnes, H.L., 1980. The kinetics of silica-water reactions. Geochem. Cosmochim. Acta 62, 1851–1863. https://doi.org/10.1016/0016-7037(80)90220-3.

Saishu, H., Okamoto, A., Tsuchiya, N., 2012. Mineralogical variation of silica induced by Al and Na in hydrothermal solutions. Am. Mineral. 97, 2060–2063. https://doi.org/10.2138/am.2012.4258.

Saishu, H., Okamoto, A., Tsuchiya, N., 2014. The significance of silica precipitation on the formation of the permeable-impermeable boundary within Earth's crust. Terra. Nova 26, 253–259. https://doi.org/10.1111/ter.12093.

Schmidt, C., Busch, B., Hilgers, C., 2020. Compaction and cementation control on bleaching in Triassic fluvial red beds, S-Germany. Z. Dtsch. Ges. Geowiss. https://doi.org/10.1127/zdgg/2020/0233.

Scott, S.W., Driesner, T., 2018. Permeability changes resulting from quartz precipitation and dissolution around upper crustal intrusions. Geofluids 1–19. https://doi.org/10.1155/2018/6957306.

Soyk, D., 2015. Diagenesis and Reservoir Quality of t/he Lower and Middle Buntsandstein (Lower Triassic), SW Germany, Naturwissenschaftlich-Mathematischen Gesamtfakultat. Ruprecht-Karls-University, Heidelberg, p. 201.

Spruženiece, L., Spath, M., Urai, J.L., Ukar, E., Selzer, M., Nestler, B., 2021. Wide-blocky veins explained by dependency of crystal growth rate on fracture surface type: insights from phase-field modeling. Geology. https://doi.org/10.1130/g48472.1.

Stanchits, S., Fortin, J., Gueguen, Y., Dresen, G., 2009. Initiation and propagation of compaction bands in dry and wet Bentheim Sandstone. Pure Appl. Geophys. 166, 843–868. https://doi.org/10.1007/s00024-009-0478-1.

Steefel, C.I., 2019. Reactive transport at the crossroads. Rev. Mineral. Geochem. 85, 1–26. https://doi.org/10.2138/rmg.2019.85.1.

Tirén, S.A., Askling, P., Wanstedt, S., 1999. Geologic site characterization for deep nuclear waste disposal in fractured rock based on 3D data visualization. Eng. Geol. 52, 319–346.

Tlili, A., Smith, D.C., Beny, J.-M., Boyer, H., 1989. A Raman microprobe study of natural micas. Mineral. Mag. 53, 165–179. https://doi.org/10.1180/minmag.1989.053.370.04.

Urai, J.L., Williams, P.F., van Roermund, H.L.M., 1991. Kinematics of crystal growth in syntectonic fibrous veins. J. Struct. Geol. 13, 823–836.

Vajdova, V., Baud, P., Wong, T.-F., 2004. Permeability evolution during localized deformation in Bentheim sandstone. J. Geophys. Res. 109, 1–15. https://doi.org/10.1029/2003JB002942.

Walderhaug, O., 1994. Precipitation rates for quartz cement in sandstones determined by fluid-inclusion microthermometry and temperature-history modeling. J. Sediment. Res. A64, 324–333. https://doi.org/10.2110/jsr.64.324.

Walton, M., 1960. Molecular diffusion rates in supercritical water vapor estimated from viscosity data. Am. J. Sci. 258, 385–401. https://doi.org/10.2475/ajs.258.6.385.

Wang, A., Freeman, J.J., Jolliff, B.L., 2015. Understanding the Raman spectral features of phyllosilicates. J. Raman Spectrosc. 46, 829–845. https://doi.org/10.1002/jrs.4680.

Warren, E.A., Smalley, P.C., Howarth, R.J., 1994. Compositional variations of North Sea formation waters. In: Warren, E.A., Smalley, P.C. (Eds.), North Sea Formation Waters Atlas. The Geological Society, London, pp. 119–208.

Wendler, F., Okamoto, A., Blum, P., 2016. Phase-field modeling of epitaxial growth of polycrystalline quartz veins in hydrothermal experiments. Geofluids 16, 211–230. https://doi.org/10.1111/gfl.12144.

Wüstefeld, P., Hilse, U., Lüders, V., Wemmer, K., Koehrer, B., Hilgers, C., 2017. Kilometer-scale fault-related thermal anomalies in tight gas sandstones. Mar. Petrol. Geol. 86, 288–303. https://doi.org/10.1016/j.marpetgeo.2017.05.015.